# Enhanced equatorial warming causes deep-tropical contraction and subtropical monsoon shift

Wenyu Zhou [1]*, Shang-Ping Xie [2] and Da Yang [1,3]

**Under anthropogenic warming, deep-tropical ascent of the intertropical convergence zone (ITCZ) is projected to contract equatorward[1–3] while subtropical descent associated with the Hadley cell edge is predicted to expand poleward[4]. These changes have important implications for regional climate[2,5–7], but their mechanisms are not well understood. Here we reveal a key role of enhanced equatorial surface warming (EEW) in driving the deep-tropical contraction and modulating the Hadley expansion. By shifting the seasonally warmed sea surface temperature equatorward, EEW reduces the meridional migration of the seasonal ITCZ and causes an annual-mean deep-tropical contraction. This process further contracts the subtropical circulation, as seen during El Niño, and counteracts the Hadley expansion caused by the global-scale warming. The EEW-induced contraction even dominates in the Northern Hemisphere early summer (June–July), when atmospheric circulation responses to the global-scale warming are weak[8]. Regionally, this alters the East Asian summer monsoon, shifting both the subtropical jet and Meiyu–Baiu rainband equatorward. Among models in Phase 5 of the Coupled Model Intercomparison Project[9], the degrees of the equatorward shift in the ITCZ, the early-summer subtropical circulation and the East Asian summer monsoon are correlated with EEW. Our results suggest that a better constraint on EEW is critical for accurate projection of tropical and subtropical climate change.**

The Hadley cell is a salient feature of Earth's atmospheric circulation. Its ascending branch in the deep tropics forms the ITCZ with converging trade winds while its subtropical descending branch marks the transition to the extratropics. Under global warming, the deep-tropical ascent is projected to contract equatorward[1–3] (referred to as 'the deep-tropical contraction'), implying profound changes in the tropical circulation, hydroclimate and radiative energy balance[2]. By contrast, the subtropical descent is predicted to expand poleward[4] (known as 'the Hadley expansion'), leading to poleward shifts of the subtropical arid regions[5], clouds[6] and tropical cyclones[7].

The deep-tropical contraction has been attributed to the enhanced meridional gradient in moisture or moist static energy (MSE). It has been argued that the enhanced moisture gradient leads to stronger dry advection and suppresses convection on the margin of deep convection[10], or that the enhanced MSE gradient causes more energy to be transported out of the deep tropics and narrows the deep-convective zone[3,11,12]. A quantitative understanding is lacking, however, with the underlying dynamic processes yet

to be revealed. The poleward edge of the Hadley cell is believed to be regulated by where the angular-momentum-conserving winds become baroclinically unstable[13–15]. This attributes the Hadley expansion to the increased static stability and deeper troposphere under global warming. The potential counteracting factors on the Hadley expansion are, however, not well understood.

The projected surface warming under increased $CO_2$ is enhanced near the Equator due to reduced evaporative damping[16] and tropical circulation slowdown[17]. The EEW is most pronounced over the Pacific and sometimes called the El Niño-like warming pattern. During El Niño, tropical rainfall moves towards the warmer equatorial Pacific[10,18], and the Hadley cell contracts equatorward[19,20]. This suggests potential effects of EEW on future ITCZ and Hadley cell changes. In contrast to El Niño, which peaks in boreal winter and easily dominates the interannual variability, EEW is most pronounced from April to July (Fig. 1) and embedded in the global-scale warming. The effect of EEW has not been sufficiently appreciated and needs to be elucidated.

Here, we show that EEW drives the deep-tropical contraction and seasonally modulates the Hadley cell and subtropical circulation. Projected tropical and subtropical circulation changes are sensitive to the magnitude of EEW. A better constraint on EEW will improve climate projections at seasonal and regional scales.

The deep-tropical contraction has often been described as the narrowing of the annual-mean deep-tropical ascent[2,3,11]. The annual-mean ascent is, however, integrated from the seasonal ITCZ that migrates north and south. This motivates us to investigate the deep-tropical contraction from a seasonal perspective[21]. The historical (HIST) and representative concentration pathway 8.5 (RCP8.5) experiments from the Coupled Model Intercomparison Project Phase 5 (CMIP5)[9] archive are used to represent the present and future warmer climates (Methods). Figure 1a shows the projected changes of the summer-mean (June–August for the Northern Hemisphere (NH) and December–February for the Southern Hemisphere (SH)) pressure vertical velocity at 500 hPa ($\omega_{500}$). Under global warming, the seasonal ITCZ, as indicated by the meridional centroid of the ascending $\omega_{500}$ (Methods), shifts equatorward with anomalous ascent (descent) equatorward (poleward) of the climatological ascent. This equatorward shift corresponds to a reduced seasonal migration of the zonal-mean ITCZ (Fig. 1b), which integrates annually into the 'deep-tropical contraction', as indicated by the narrowing in the distance between the annual-mean peak ascent in each hemisphere (Fig. 1c).

The seasonal ITCZ generally sits over the warmest sea surface temperature (SST). With enhanced equatorial warming, the

[1]Lawrence Berkeley National Laboratory, Berkeley, CA, USA. [2]University of California, San Diego, La Jolla, CA, USA. [3]University of California, Davis, Davis, CA, USA. *e-mail: wenyuzhou@lbl.gov
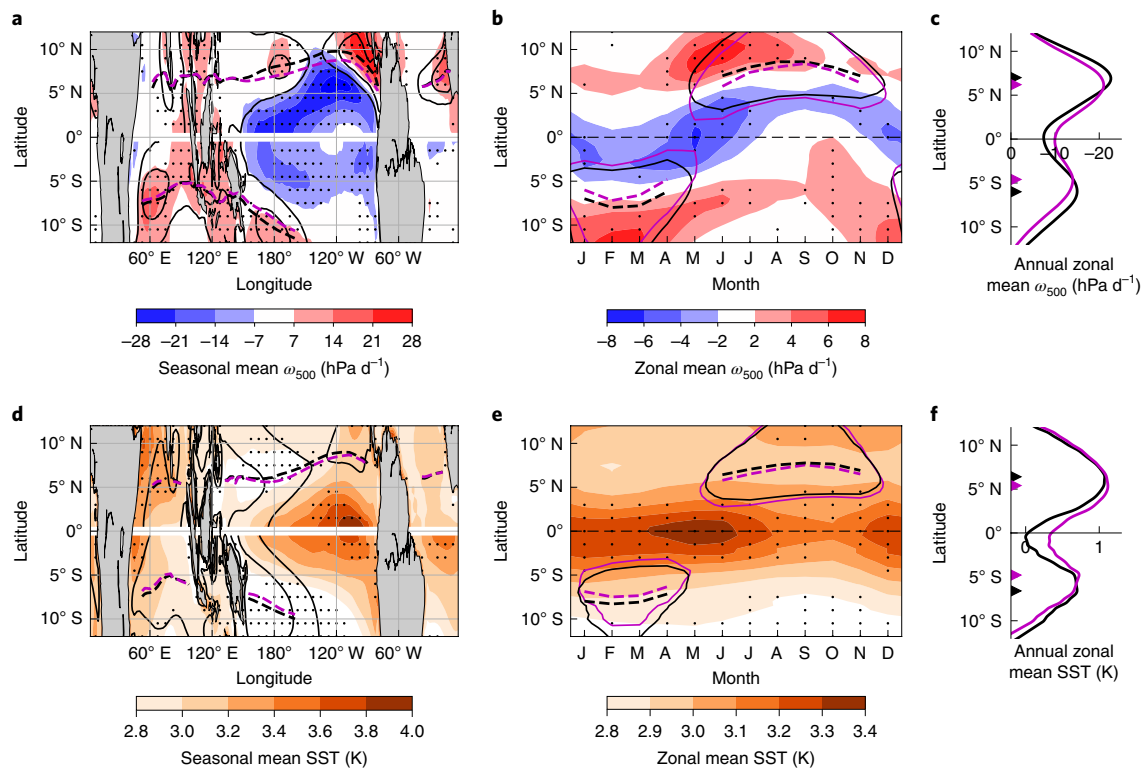
**Fig. 1 | Deep-tropical contraction integrated from equatorward-shifted seasonal ITCZ driven by EEW. a**, Spatial changes in the summer-mean (June–August for NH and December–February for SH) pressure vertical velocity at 500 hPa ($\omega_{500}$) from HIST to RCP8.5. The HIST climatology is shown in grey contours. The meridional centroids of the ascending $\omega_{500}$ are shown in dashed lines (black for HIST and magenta for RCP8.5). **b**, Seasonal climatologies (contours at −22 hPa d$^{-1}$; black for HIST and magenta for RCP8.5) and changes under global warming (shading) of the zonal-mean $\omega_{500}$. The meridional centroids are shown in dashed lines. **c**, Annual- and zonal-mean $\omega_{500}$ climatologies (black for HIST and magenta for RCP8.5). The triangle symbols indicate the latitudes of the annual-mean peak ascent. **d–f**, Same as **a–c** but for the SST. The seasonal climatologies in **e** (contours at 1.2 K) and the annual-mean zonal-mean in **f** are shown for the SST anomaly relative to the 20° S–20° N ocean mean. The meridional centroids in **d** are computed from the positive SST anomaly. Stippling in **a** and **b** indicates that at least 75% (15 out of 20) of the models agree on the sign of the changes while stippling in **d** and **e** indicates that at least 75% of the models agree on the sign of the relative changes to the 20° S–20° N ocean mean.

meridional centroid of the seasonally warmed SST (warmer than the 20° S–20° N ocean mean) shifts equatorward (Fig. 1d and Supplementary Fig. 1), leading to the equatorward shift of the seasonal ITCZ. In the zonal mean (Fig. 1b,e), the ITCZ shift is most pronounced from April to July, a period when EEW is strongest with significant equatorward shift in the warm-SST centroid, and weak in September–October, when EEW is less pronounced. The annual-mean deep-tropical contraction (Fig. 1c) is consistently indicated by an equatorward contraction in the relatively warm SST (Fig. 1f).

The effect of EEW on the equatorward ITCZ shift can be rigorously understood from its control on the large-scale thermodynamic and energetic changes. According to the convective quasi-equilibrium theory[22], the peak ascent generally follows the peak of the surface equivalent potential temperature[23] ($\theta_e$). From the quasi-equilibrium energetic perspective[24] (Methods), the large-scale ascent is determined by the ratio between the energy input into the atmosphere column ($F_A$) and the gross moist stability (GMS). The equatorward ITCZ shift is consistently indicated by the equatorward shifts in the meridional centroids of $\theta_e$ and $\frac{F_A}{\text{GMS}}$ (Supplementary Fig. 1). The shift in $\theta_e$ is related to the enhanced equatorial $\theta_e$ increase, which is directly driven by EEW (through both the dry and moist parts) and amplified by relative-humidity feedback from the ITCZ shift itself (Supplementary Fig. 2). The shift in $\frac{F_A}{\text{GMS}}$ is driven by the equatorward shift of GMS due to EEW (Supplementary Fig. 3) and amplified by cloud longwave feedback on $F_A$ in association with the ITCZ shift (Supplementary Fig. 4).

The essential role of EEW in driving the deep-tropical contraction can be further demonstrated from a denial experiment and the intermodel spread. Atmospheric Model Intercomparison Project (AMIP) experiments forced with prescribed SST (Methods) indicate that the equatorward shift of the seasonal ITCZ and the resulting annual-mean contraction are only present when EEW is included in the warming pattern (Fig. 2a,b) and are absent when forced with uniform warming (Fig. 2c,d). Among CMIP5 models, the equatorward shift of the seasonal ITCZ is correlated with the magnitude of EEW (Methods), increasing with EEW at ~4° K$^{-1}$ (Fig. 2e), and the degree of the annual-mean deep-tropical contraction (Methods) can be directly inferred from the equatorward shift of the seasonal ITCZ (Fig. 2f).

We now look beyond the deep tropics and investigate the effect of EEW on the subtropical circulation. The El Niño event provides a good analogy for us to consider the EEW effect. During El Niño, as the ITCZ shifts equatorward in the summer hemisphere, the Hadley cell contracts in both hemispheres, with equatorward shifts in the subtropical jet and descent (Supplementary Figs. 5 and 6). While the full dynamics remain to be investigated, previous studies using idealized simulations suggest that the Hadley contraction is dynamically linked with the ITCZ shift[25–27] through subtropical adjustments[28–30]. For the cross-equatorial winter Hadley cell, the angular-momentum-conservation theory explains that an equatorward ITCZ shift would intensify the subtropical jet and thus shift the eddy–momentum convergence and subtropical descent
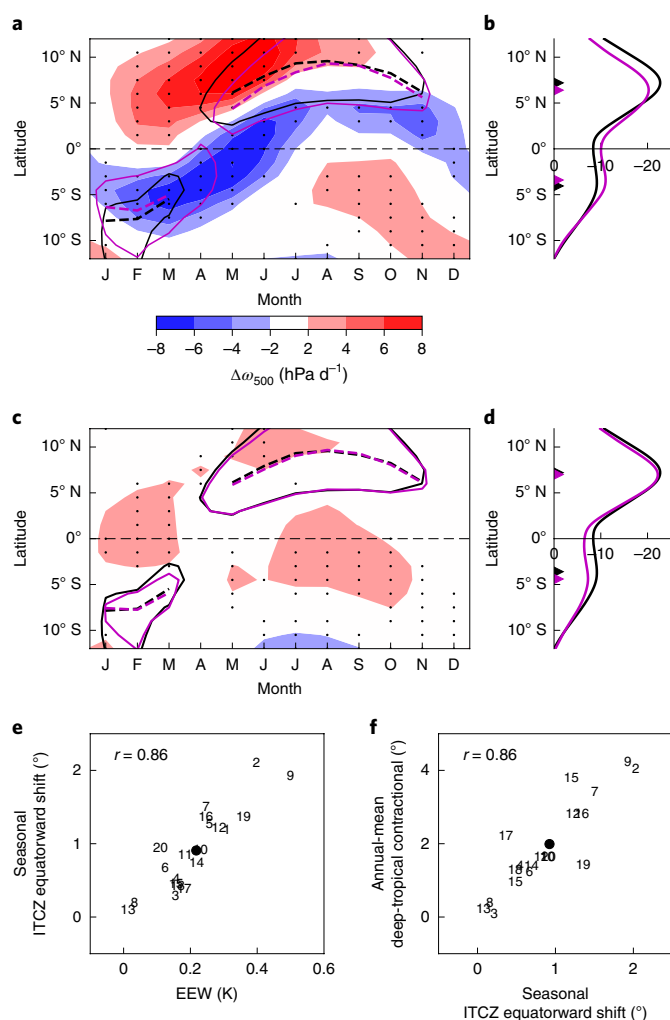
**Fig. 2 | Denial experiment and intermodel spread of the deep-tropical contraction. a**, Seasonal responses (shading) of the zonal-mean $\omega_{500}$ to a patterned warming with EEW included (from AMIP to AMIPFuture). The climatologies are shown in contours, and the meridional centroids are indicated by dashed lines (black for AMIP and magenta for AMIPFuture). **b**, Annual- and zonal-mean $\omega_{500}$ climatologies (black for AMIP and magenta for AMIPFuture). The triangle symbols indicate the latitudes of the annual-mean peak ascent. Stippling indicates where at least 75% (15 out of 20) of the models agree on the sign of the differences. **c,d**, Same as **a,b** but for the response to a uniform warming of 4 K (from AMIP to AMIP4K). **e**, Intermodel scatterplot between EEW and the equatorward shift of the seasonal ITCZ (reduced seasonal ITCZ migration). **f**, Intermodel scatterplot between the equatorward shift of the seasonal ITCZ and the annual-mean deep-tropical contraction (narrowing in the distance between the annual-mean peak ascents). Individual models are indexed (Methods), and the black dot shows the ensemble mean. Pearson correlation coefficients are 0.86 for both **e** and **f**.

equatorward[25,26]. For the summer cell that sits in one hemisphere, the subtropical jet and descent shift equatorward as they appear to

move in the same direction as the ITCZ. Under global warming, the SH Hadley cell expands nearly uniformly throughout the year (Fig. 3a), but the expansion in the NH shows a strong seasonal variation[25] (Fig. 3b). In particular, the Hadley expansion is substantially reduced or even reversed into an equatorward contraction in June–July (see Supplementary Fig. 7 for consistent equatorward shifts in the subtropical jet and hydrological imbalance). This early-summer Hadley contraction is probably caused by the EEW effect.

To confirm and understand the EEW effect, we have conducted paired warming experiments using the Geophysical Fluid Dynamics Laboratory (GFDL) AM2.1 atmosphere model (Methods): one forced with the surface warming derived from RCP8.5 (GW) and the other with EEW removed from the warming pattern (GWnoEEW). Changes from GWnoEEW to GW then illustrate the effect of EEW. The SH Hadley expansion is considerably reduced from GWnoEEW to GW in April–June (Fig. 3c) due to the seasonally strengthened EEW (Fig. 1e). The most pronounced effect of EEW is found in the NH June–July: the Hadley expansion in GWnoEEW is reversed into an equatorward contraction in GW (Fig. 3d). This confirms that EEW drives the projected early-summer Hadley contraction. A consistent summer contraction is found from the hydrological boundary of the tropics (Supplementary Fig. 8).

The season- and hemisphere-dependent effects of EEW can be understood from the counterplay between the global-scale warming (GWnoEEW) and EEW. Figure 3e–h shows the change of the 250 hPa zonal winds ($U_{250}$) in GWnoEEW and in response to EEW (measured as GW – GWnoEEW) in early summer (June–July) and autumn (September–November). In the NH early summer, atmospheric circulation changes in GWnoEEW are weak due to the tug of war on the land–sea thermal contrast between radiative forcing and ocean warming[8] (Fig. 3e), while the strong EEW induces a notable equatorward shift in the zonal wind pattern (Fig. 3f). The EEW effect thus dominates and causes the Hadley contraction. In the NH winter, however, the EEW-induced Hadley contraction is weak. As the subtropical jet and descent are much stronger in winter, circulation changes induced by EEW appear less effective in driving an equatorward shift (Supplementary Figs. 7 and 9d). This weak Hadley contraction in winter may be model dependent. In the SH, circulation changes in GWnoEEW are persistently strong and dominate over those due to EEW. In autumn, the weak EEW induces weak circulation responses (Fig. 3h) that are dominated by those due to the global-scale warming (Fig. 3g). The season-dependent effect of EEW causes the controlling factors of the NH Hadley changes to vary between early summer and autumn. With negligible influences from EEW, the Hadley expansion in autumn projected by individual models is correlated with the extratropical warming (ETW$_{SON}$; Methods), increasing with ETW$_{SON}$ at ~0.9° K$^{-1}$ (Fig. 3i), while the relative Hadley contraction in early summer is controlled by the early-summer EEW relative to the NH subtropics (EEW$_{JJ}^{NH}$; Methods), increasing with EEW$_{JJ}^{NH}$ at ~6° K$^{-1}$ (Fig. 3j).

The Hadley cell describes the zonal-mean circulation. It is not clear to what extent the Hadley cell changes could be realized at regional scales, in particular, for the NH summer when the Hadley cell is weak and longitudinally confined monsoons dominate. Here, we have identified a consistent equatorward shift in the East Asian subtropical summer monsoon (EASM). Characterized by the Meiyu–Baiu rainband, the EASM brings the much-needed

**Fig. 3 | Seasonal-dependent contraction effect of EEW. a,b**, Seasonal Hadley expansion ($\Delta\phi^{HC}$) under global warming in the SH (**a**) and NH (**b**), respectively. The bars show the ensemble mean of CMIP5, and the error bars indicate the intermodel standard deviation. **c,d**, Same as **a,b** but for seasonal Hadley expansion in the GFDL-AM2.1 warming experiments. The unfilled and filled bars show responses to GWnoEEW and GW, respectively. **e,f**, June–July changes of the 250 hPa zonal winds ($\Delta U_{250}$) in response to GWnoEEW (**e**) and EEW (**f**). The purple contours show the $U_{250}$ seasonal climatology. The black box highlights the area of the EASJ. **g,h**, Same as **e,f** but for September–November. **i**, Intermodel scatterplot between ETW$_{SON}$ and $\Delta\phi^{HC}_{SON}$ in the NH. Pearson correlation coefficient $r$ is 0.76. **j**, Intermodel scatterplot between the June–July EEW relative to the NH subtropics (EEW$_{JJ}^{NH}$) and the NH Hadley contraction in June–July relative to the annual-mean expansion ($\Delta\phi^{NH}_{JJ}$). Pearson correlation coefficient $r$ is −0.65.

summer rainfall to more than one billion people. The Meiyu–Baiu rainband is closely coupled to the upper-level East Asian subtropical jet (EASJ)[31,32], with the large-scale ascent located just equa-

torward of the EASJ. As highlighted by the black box in Fig. 3e,f (Supplementary Fig. 10 for a zoom-in picture), the latitude of the EASJ barely changes in GWnoEEW (Fig. 3e) but shifts equatorward
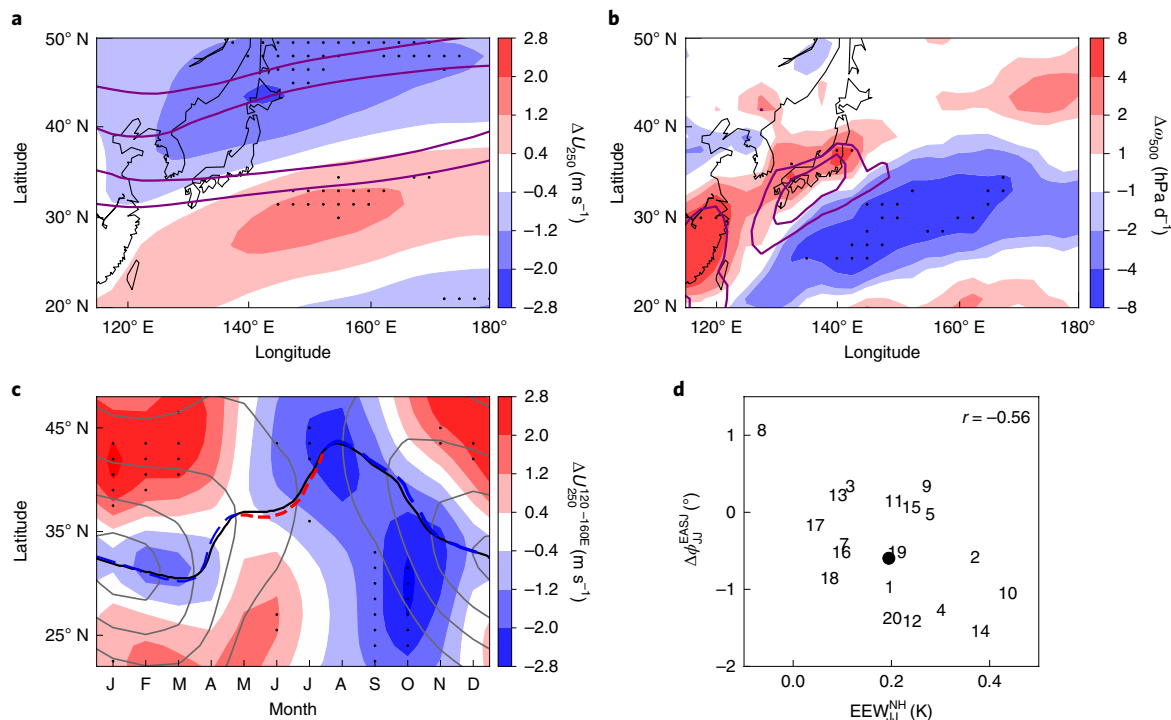


**NATURE CLIMATE CHANGE** | www.nature.com/natureclimatechange
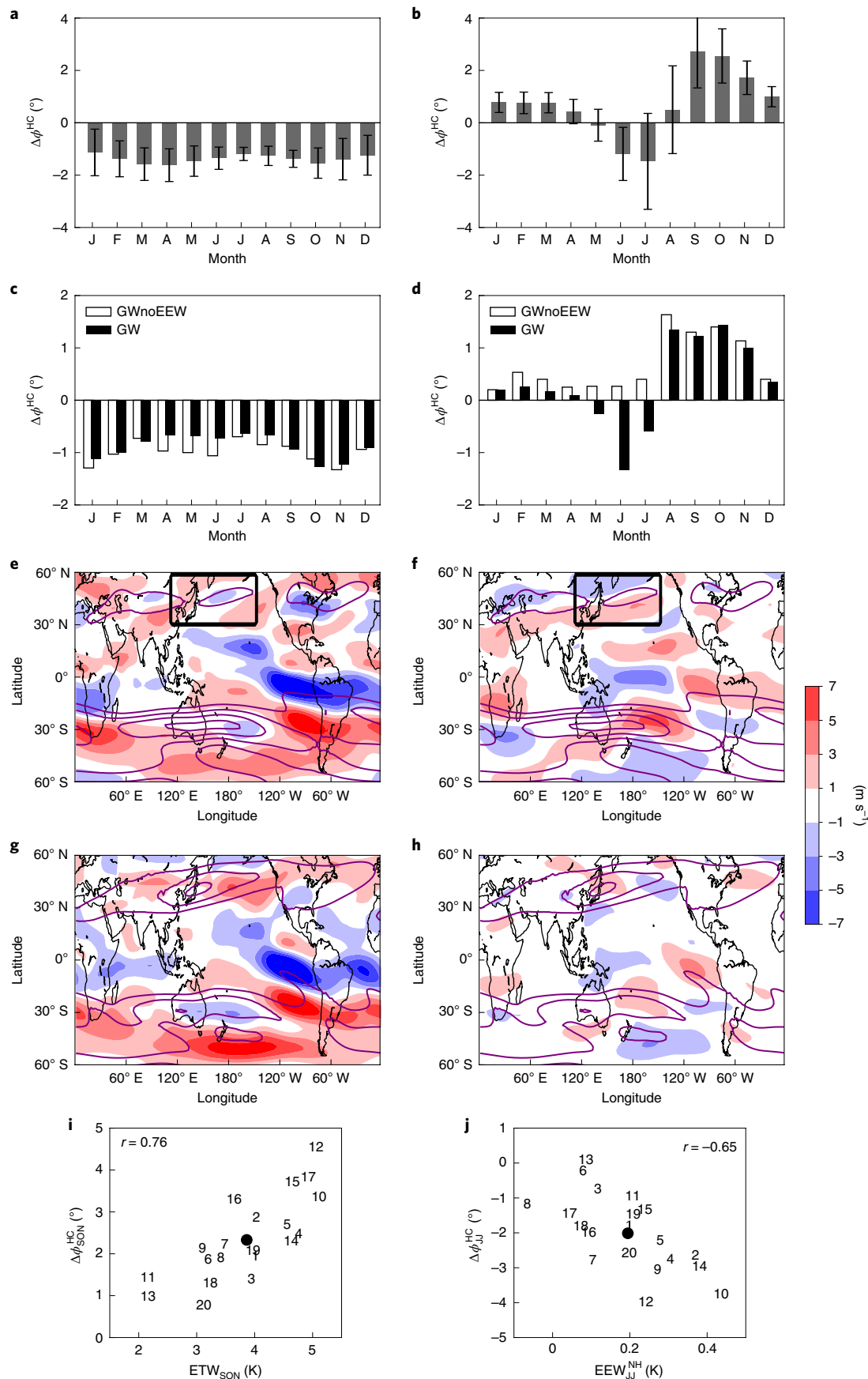
**Fig. 4 | Equatorward shift of the EASM controlled by EEW. a,b**, Spatial changes of the early-summer (June–July) $U_{250}$ (**a**) and $\omega_{500}$ (**b**) from HIST to RCP8.5. The HIST climatology is shown in purple contours. Stippling indicates that at least 75% (15 out of 20) of the models agree on the sign of the changes. **c**, Seasonal changes of the EASJ ($U_{250}$ averaged from 120° E to 160° E) from HIST to RCP8.5. The climatological EASJ is shown in grey contours. The jet core is shown in the solid black line for HIST and in the dashed coloured line for RCP8.5. **d**, Intermodel scatterplot of the June–July EEW relative to the NH subtropics ($EEW_{JJ}^{NH}$) and the EASJ shift in June–July relative to the annual mean ($\Delta\phi_{JJ}^{EASJ}$). The Pearson correlation coefficient $r$ is −0.56. The outlier CCSM4 model (which predicts an ~4° equatorward shift in EASJ while the second largest is only ~1.5°) is excluded in both the ensemble-mean projection (**a**–**c**) and the intermodel scatterplot (**d**).

with EEW (Fig. 3f). The CMIP5 ensemble-mean projection indicates a consistent equatorward shift in both the EASJ (Fig. 4a) and the Meiyu–Baiu rainband (Fig. 4b) under global warming. The EASJ shifts equatorward only in early summer, in contrast to a general poleward shift in other seasons (Fig. 4c). The crucial role of EEW can be further seen from the intermodel spread. After excluding one outlier model (CCSM4), which predicts a spurious 4° shift, the relative equatorward shift of the EASJ in early summer is correlated with $EEW_{JJ}^{NH}$, increasing with $EEW_{JJ}^{NH}$ at ~4° K$^{-1}$ (Fig. 4d).

In summary, we have identified EEW as the driver of the deep-tropical contraction and as a key seasonal modulator of the subtropical circulation. In the deep tropics, EEW shifts the warm SST band towards the Equator so that the seasonal ITCZ shifts equatorward, leading to a reduced meridional migration of the ITCZ and an annual-mean deep-tropical contraction. The equatorward ITCZ shift due to EEW refines the 'warmer get wetter' paradigm[33] for understanding the tropical circulation changes: regional circulation changes may not scale with local warming but rather result from a shift of the climatological pattern controlled by remote relative warming. ITCZ studies over the past two decades have extensively studied its annual-mean interhemispheric asymmetry[34–36]. Our study here emphasizes a different metric: the seasonal migration. The reduced ITCZ migration changes the seasonal deep-tropical circulation and is likely to affect tropical weather patterns such as easterly waves and cyclogenesis. Beyond the deep tropics, the counterplay between EEW and the global-scale warming induces a season-dependent change in the subtropical circulation. Over East Asia in early summer, in particular, EEW causes an equatorward shift in both the westerly jet and the Meiyu–Baiu rainband. This illustrates the importance of EEW in regulating the subtropical

climate at regional and seasonal scales. While all CMIP5 models predict an EEW, considerable uncertainty exists regarding the magnitude. Such uncertainty has far-reaching impacts on the projected tropical and subtropical seasonal climate. Further studies are needed to constrain the magnitude uncertainty of EEW, investigate the impacts of the ITCZ equatorward shift on tropical weather patterns and better understand the dynamics of the season-dependent subtropical circulation changes.

## Online content

Any methods, additional references, Nature Research reporting summaries, source data, statements of code and data availability and associated accession codes are available at https://doi.org/10.1038/s41558-019-0603-9.

## References

1. Huang, P., Xie, S.-P., Hu, K., Huang, G. & Huang, R. Patterns of the seasonal response of tropical rainfall to global warming. *Nat. Geosci.* **6**, 357–361 (2013).
2. Lau, W. K. M. & Kim, K.-M. Robust Hadley circulation changes and increasing global dryness due to CO₂ warming from CMIP5 model projections. *Proc. Natl. Acad. Sci. USA* **112**, 3630–3635 (2015).
3. Byrne, M. P. & Schneider, T. Narrowing of the ITCZ in a warming climate: physical mechanisms. *Geophys. Res. Lett.* **43**, 11350–11357 (2016).
4. Lu, J., Vecchi, G. A. & Reichler, T. Expansion of the Hadley cell under global warming. *Geophys. Res. Lett.* **34**, L06805 (2007).
5. Scheff, J. & Frierson, D. M. W. Robust future precipitation declines in CMIP5 largely reflect the poleward expansion of model subtropical dry zones. *Geophys. Res. Lett.* **39**, L18704 (2012).

6.   Norris, J. R. et al. Evidence for climate change in the satellite cloud record. *Nature* **536**, 72–75 (2016).
7.   Kossin, J. P., Emanuel, K. A. & Vecchi, G. A. The poleward migration of the location of tropical cyclone maximum intensity. *Nature* **509**, 349–352 (2014).
8.   Shaw, T. A. & Voigt, A. Tug of war on summertime circulation between radiative forcing and sea surface warming. *Nat. Geosci.* **8**, 560–566 (2015).
9.   Taylor, K. E., Stouffer, R. J. & Meehl, G. A. An overview of CMIP5 and the experiment design. *Bull. Am. Meteorol. Soc.* **93**, 485–498 (2012).
10.  Neelin, J. D., Chou, C. & Su, H. Tropical drought regions in global warming and El Niño teleconnections. *Geophys. Res. Lett.* **30**, 2275 (2003).
11.  Byrne, M. P. & Schneider, T. Energetic constraints on the width of the intertropical convergence zone. *J. Clim.* **29**, 4709–4721 (2016).
12.  Byrne, M. P., Pendergrass, A. G., Rapp, A. D. & Wodzicki, K. R. Response of the intertropical convergence zone to climate change: location, width, and strength. *Curr. Clim. Change Rep.* **4**, 355–370 (2018).
13.  Held, I. M. The general circulation of the atmosphere. In *Proc. 2000 Program of Study in Geophysical Fluid Dynamics* 1–54 (Woods Hole Oceanographic Institution, 2000).
14.  Walker, C. C. & Schneider, T. Eddy influences on Hadley circulations: simulations with an idealized GCM. *J. Atmos. Sci.* **63**, 3333–3350 (2006).
15.  Frierson, D. M. W., Lu, J. & Chen, G. Width of the Hadley cell in simple and comprehensive general circulation models. *Geophys. Res. Lett.* **34**, L18804 (2007).
16.  Liu, Z., Vavrus, S., He, F., Wen, N. & Zhong, Y. Rethinking tropical ocean response to global warming: the enhanced equatorial warming. *J. Clim.* **18**, 4684–4700 (2005).
17.  Vecchi, G. A. & Soden, B. J. Global warming and the weakening of the tropical circulation. *J. Clim.* **20**, 4316–4340 (2007).
18.  Dai, A. & Wigley, T. M. L. Global patterns of ENSO-induced precipitation. *Geophys. Res. Lett.* **27**, 1283–1286 (2000).
19.  Seager, R., Harnik, N., Kushnir, Y., Robinson, W. & Miller, J. Mechanisms of hemispherically symmetric climate variability. *J. Clim.* **16**, 2960–2978 (2003).
20.  Lu, J., Chen, G. & Frierson, D. M. W. Response of the zonal mean atmospheric circulation to El Niño versus global warming. *J. Clim.* **21**, 5835–5851 (2008).
21.  Donohoe, A., Atwood, A. R. & Byrne, M. P. Controls on the width of tropical precipitation and its contraction under global warming. *Geophys. Res. Lett.* https://doi.org/10.1029/2019GL082969 (2019).
22.  Emanuel, K. A. On thermally direct circulations in moist atmospheres. *J. Atmos. Sci.* **52**, 1529–1534 (1995).
23.  Privé, N. C. & Plumb, R. A. Monsoon dynamics with interactive forcing. Part I: axisymmetric. *Stud. J. Atmos. Sci.* **64**, 1417–1430 (2007).
24.  Neelin, J. D. & Held, I. M. Modeling tropical convergence based on the moist static energy budget. *Mon. Weather Rev.* **115**, 3–12 (1987).
25.  Kang, S. M. & Lu, J. Expansion of the Hadley cell under global warming: winter versus summer. *J. Clim.* **25**, 8387–8393 (2012).
26.  Watt-Meyer, O. & Frierson, D. M. W. ITCZ width controls on Hadley cell extent and eddy-driven jet position and their response to warming. *J. Clim.* **32**, 1151–1166 (2018).
27.  Hilgenbrink, C. C. & Hartmann, D. L. The response of Hadley circulation extent to an idealized representation of poleward ocean heat transport in an aquaplanet GCM. *J. Clim.* **31**, 9753–9770 (2018).
28.  Chen, G., Plumb, R. A. & Lu, J. Sensitivities of zonal mean atmospheric circulation to SST warming in an aqua-planet model. *Geophys. Res. Lett.* **37**, L12701 (2010).
29.  Tandon, N. F., Gerber, E. P., Sobel, A. H. & Polvani, L. M. Understanding Hadley cell expansion versus contraction: insights from simplified models and implications for recent observations. *J. Clim.* **26**, 4304–4321 (2012).
30.  Sun, L., Chen, G. & Lu, J. Sensitivities and mechanisms of the zonal mean atmospheric circulation response to tropical warming. *J. Atmos. Sci.* **70**, 2487–2504 (2013).
31.  Sampe, T. & Xie, S.-P. Large-scale dynamics of the Meiyu-Baiu rainband: environmental forcing by the westerly jet. *J. Clim.* **23**, 113–134 (2010).
32.  Chen, J. & Bordoni, S. Orographic effects of the Tibetan Plateau on the East Asian summer monsoon: an energetic perspective. *J. Clim.* **27**, 3052–3072 (2014).
33.  Xie, S.-P. et al. Global warming pattern formation: sea surface temperature and rainfall. *J. Clim.* **23**, 966–986 (2010).
34.  Broccoli, A. J., Dahl, K. A. & Stouffer, R. J. Response of the ITCZ to Northern Hemisphere cooling. *Geophys. Res. Lett.* **33**, L01702 (2006).
35.  Kang, S. M., Held, I. M., Frierson, D. M. W. & Zhao, M. The response of the ITCZ to extratropical thermal forcing: idealized slab-ocean experiments with a GCM. *J. Clim.* **21**, 3521–3532 (2008).
36.  Schneider, T., Bischoff, T. & Haug, G. H. Migrations and dynamics of the intertropical convergence zone. *Nature* **513**, 45–53 (2014).

## Author contributions

W.Z. designed the research, conducted the simulations and analysed the results. S.-P.X. and D.Y. contributed to improving the analysis and interpretation. W.Z. wrote the first draft, and all authors discussed and edited the paper.

## Competing interests

The authors declare no competing interests.

## Additional information

**Supplementary information** is available for this paper at https://doi.org/10.1038/s41558-019-0603-9.

**Correspondence and requests for materials** should be addressed to W.Z.

**Peer review information** *Nature Climate Change* thanks Michael Byrne and the other, anonymous, reviewer(s) for their contribution to the peer review of this work.

**Reprints and permissions information** is available at www.nature.com/reprints.

**Publisher's note** Springer Nature remains neutral with regard to jurisdictional claims in published maps and institutional affiliations.

## Methods

**CMIP.** The projected future changes in response to global warming are illustrated using the HIST and RCP8.5 experiments from 20 coupled global climate models that contribute to the CMIP5: ACCESS1-0 (1), ACCESS1-3 (2), bcc-csm1-1 (3), BNU-ESM (4), CanESM2 (5), CCSM4 (6), CESM1-CAM5 (7), CNRM-CM5 (8), CSIRO-Mk3.6.0 (9), GFDL-CM3 (10), GISS-E2-R (11), HadGEM2-ES (12), inmcm4 (13), IPSL-CM5A-LR (14), IPSL-CM5B-LR (15), MIROC5 (16), MIROC-ESM (17), MPI-ESM-LR (18), MRI-CGCM3 (19) and NorESM1-M (20). The numbers in parenthesis denote individual models in the scatterplot figures. The 1979–2005 mean in HIST is used to represent the present climatology, the 2080–2100 mean in RCP8.5 is used to represent the future warmer climatology and their differences represent the changes under global warming.

**AMIP.** We use outputs from eight atmosphere models that have a complete set of AMIP, AMIP4K and AMIPFuture experiments in CMIP5 to help understand the effect of the patterned warming. They are bcc-csm1-1, CanAM4, CCSM4, CNRM-CM5, IPSL-CM5A-LR, MIROC5, MPI-ESM-LR, MRI-CGCM3. In AMIP, the atmosphere models are forced with observed SST and sea ice. In AMIP4K, a spatially uniform SST warming of 4 K is superimposed on the observed SST. AMIPFuture uses the spatially patterned SST warming derived from the CMIP3 1pctCO2 simulation (averaged around the time when $CO_2$ is quadrupled), which features an enhanced equatorial warming similar to those projected in RCP8.5.

In the main result, we do not use the differences between AMIP4K and AMIPFuture to illustrate the effect of EEW on the Hadley expansion. The prescribed extratropical warming is very different between AMIP4K and AMIPFuture so that their comparison may not isolate the effect of EEW. Nevertheless, a similar plot to Fig. 3d does indicate an early-summer Hadley contraction from AMIP4K to AMIPFuture (Supplementary Fig. 11), supporting the contraction effect from EEW.

**GFDL-AM2.1 simulations.** To investigate the effect of EEW on the Hadley expansion, we have conducted idealized warming experiments using the GFDL-AM2.1 (ref. [37]) atmosphere model. The control simulation is forced with the climatological SST averaged from 1980 to 2005. A global uniform $CO_2$ concentration of 355 ppm is used, and all other trace gases for radiation computation are fixed at the values of the year 1990. The GW (global warming) simulation is forced with the climatological SST plus the SST warming pattern (2080–2100 minus 1979–2005) derived from the ensemble-mean RCP8.5 projection and with an increased $CO_2$ concentration of 800 ppm. The enhanced SST warming in the equatorial Pacific (10° S–10° N, 140° E–80° W) is artificially removed in the GWnoEEW (global warming without enhanced deep-tropical warming) simulation by linear interpolation between 10° S and 10° N. The changes from GWnoEEW to GW thus measure the effect of EEW on future changes. All simulations are run for 55 yr, and the last 50 yr are used for analysis.

**ERA-interim reanalysis dataset.** The El Niño/Southern Oscillation is a mode of natural variability of climate, with equatorial warming/cooling over the equatorial East Pacific. The monthly mean fields (1979–2018) from the ERA-interim reanalysis dataset[38] are used to compute the El Niño and La Niña composites and illustrate the responses of the seasonal atmospheric circulation to the El Niño/Southern Oscillation (Supplementary Figs. 5 and 6).

All model and reanalysis outputs have been interpolated to a common grid of 1° × 1° (latitude × longitude) resolution before analysis. The location metrics such as the poleward edge of the Hadley cell and the location of the peak ascent are computed after further interpolating the large-scale ascent to a finer resolution of 0.2°.

**Meridional centroids.** The meridional centroid of the ITCZ is defined as:

$$\phi^{\text{ITCZ}} = \frac{\int_0^{\phi_0} \omega_{500}^{\uparrow} \phi \, d\phi}{\int_0^{\phi_0} \omega_{500}^{\uparrow} \, d\phi}$$

where $\omega_{500}^{\uparrow}$ is the ascending $\omega_{500}$ (the descending $\omega_{500}$ is masked as 0), $\phi$ is the latitude and $\phi_0 = \pm 12.5°$ for the NH and SH.

The meridional centroid of $\frac{F_A}{\text{GMS}}$ is defined as:

$$\phi^{\frac{F_A}{\text{GMS}}} = \frac{\int_0^{\phi_0} \frac{F_A}{\text{GMS}}^+ \phi \, d\phi}{\int_0^{\phi_0} \frac{F_A}{\text{GMS}}^+ \, d\phi}$$

where $\frac{F_A}{\text{GMS}}^+$ refers to the positive $\frac{F_A}{\text{GMS}}$ (the negative value is masked as 0).

For variables such as SST, $\theta_e$, GMS and $F_A$, their meridional centroids are defined as:

$$\phi^{\chi} = \frac{\int_0^{\phi_0} \chi' \phi \, d\phi}{\int_0^{\phi_0} \chi' \, d\phi}$$

where $\chi$ refers to SST, $\theta_e$, GMS or $F_A$ and $\chi'$ is the positive (negative for GMS) anomaly relative to the 20° S–20° N ocean mean.

**Thermodynamic and energetic controls.** The surface equivalent potential temperature ($\theta_e$) is computed[39] using the 2 m air temperature, humidity and surface pressure. From the quasi-equilibrium energetic perspective, the energy input into the atmosphere column from surface fluxes and radiation is balanced by the energy transported out by circulation so that the large-scale ascent is determined by the ratio between the atmospheric energy input ($F_A$) and the GMS. The value $F_A$ is computed as the sum of radiative forcing and surface energy fluxes, that is:

$$F_A = R^{\text{TOA}} - R^{\text{SFC}} + \text{SFX}$$

where $R^{\text{TOA}}$ is the net radiative flux into the atmosphere at the top of the atmosphere, $R^{\text{SFC}}$ is the net radiative flux into the surface and SFX is the surface turbulent fluxes (latent + sensible) into the atmosphere. GMS quantifies the efficiency of the MSE export by circulations associated with the ascent. Here GMS is measured as the difference in MSE (in the unit of temperature after normalizing with the isobaric specific heat capacity of air) between the upper (150–300 hPa) and lower (825–975 hPa) troposphere. Such a simple estimate of GMS does not involve the vertical profile of the pressure velocity, as originally defined in ref. [23], and the resulting $\frac{F_A}{\text{GMS}}$ well captures the spatial changes in $\omega_{500}$. By using $\frac{F_A}{\text{GMS}}$ instead of $\frac{F_A - d\int \text{MSE}}{\text{GMS}}$, we have neglected the transient energy change of the atmosphere column, $d\int \text{MSE}$, which is small over the summer and winter seasons. Including this term makes negligible improvement to Supplementary Fig. 1j–l.

**SST metrics.** EEW (Fig. 2e) is measured as the annual-mean SST warming averaged between 5° S and 5° N relative to the annual-mean tropical-mean SST warming averaged from 20° S to 20° N. $\text{ETW}_{\text{SON}}$ (Fig. 3i) is computed as the mean SST warming averaged from 10° N to 70° N during September–November. $\text{EEW}_{\text{JJ}}^{\text{NH}}$ (Figs. 3j and 4d) is measured as the relative SST warming averaged between 5° S and 5° N to the NH subtropical warming averaged from 5° N to 20° N during June–July.

**The equatorward shift of the seasonal ITCZ and the annual-mean deep-tropical contraction.** The equatorward shift of the seasonal ITCZ (Fig. 2e,f), that is, the reduced seasonal migration of the ITCZ, is measured as the decrease in the standard deviation of the latitudes of the monthly peak ascent. The annual-mean deep-tropical contraction (Fig. 2f) is measured as the narrowing in the distance between the annual-mean peak ascents. A strong correlation between the reduced seasonal ITCZ migration and the annual-mean deep-tropical contraction is found here using the latitude of the peak ascent. A weaker correlation is found in ref. [3] using the latitude of the maximum/minimum zonal-mean mass streamfunction where the vertical velocity changes from ascent to descent.

**The Hadley expansion/contraction.** The Hadley expansion/contraction (Fig. 3) is measured by the meridional shift in the Hadley cell poleward edge, which is identified for each month as the zero crossing of the zonal-mean streamfunction at 500 hPa.

**Meridional shift of the EASJ.** The EASJ shift (Fig. 4d) is measured by the meridional shift in the EASJ latitude, which is identified for each month as the mean latitude of the maximum westerly $U_{250}$ from 120° E to 160° E.

## Data availability

The data supporting the findings of this study are available within the manuscript and its supplementary information. Data associated with the GFDL-AM2.1 simulations are available at https://github.com/wenyuz/EEW. The AMIP and CMIP outputs can be obtained from the CMIP5 archive, accessed through http://www.ipcc-data.org/sim/gcm_monthly/AR5/Reference-Archive.html.

## Code availability

The data analysis code is available from the corresponding author on request.

## References

37. GAMDT. The new GFDL global atmosphere and land model AM2-LM2: evaluation with prescribed SST simulations. *J. Clim.* **17**, 4641–4673 (2004).
38. Dee, D. P. et al. The ERA-Interim reanalysis: configuration and performance of the data assimilation system. *Q. J. R. Meteorol. Soc.* **137**, 553–597 (2011).
39. Bolton, D. The computation of equivalent potential temperature. *Mon. Weather Rev.* **108**, 1046–1053 (1980).